Materials Advances

ROYAL SOCIETY OF CHEMISTRY

PAPER

View Article Online
View Journal | View Issue

Cite this: *Mater. Adv.*, 2023, 4, 3839

High energy density liquid state asymmetric supercapacitor devices using Co–Cr–Ni–Fe–Mn high entropy alloy†

Gobinda C. Mohanty,[a] Chinmayee C. Gowda,[a] Pooja Gakhad,[b] M. Sanjay,[c] Suman Sarkar,[d] Koushik Biswas,*[ac] Abhishek Singh*[b] and Chandra S. Tiwary*[ac]

Received 25th June 2023,
Accepted 27th July 2023

DOI: 10.1039/d3ma00327b

rsc.li/materials-advances

For satisfying the ever-growing need in novel material search for energy storage applications, high entropy alloys (HEAs) have been explored recently. A simple induction melting method was used to synthesize the CoCrNiFeMn bulk HEA sample that was later ball-milled to obtain nanoparticles. The dimension reduction provided an increased surface area for sample usage in supercapacitor applications. The highest specific capacitance of 386.66 F g^{-1} was obtained at 5 mV s^{-1} in an aqueous 3 M KOH electrolyte in a three-electrode system. We also studied the contribution of d-band electrons from the metals for electrochemical interaction in the system through DFT calculations. The liquid state CoCrNiFeMn//activated carbon (AC) asymmetric supercapacitor (ASC) device was fabricated, and the energy stored was used to glow a 1.5 V LED device. The energy density of the ASC device was 21 W h kg^{-1} at a power density of 307 W kg^{-1}, which is one of the first reports on HEA-based liquid-state asymmetric devices.

Introduction

Supercapacitors have been the primary choice for energy storage systems owing to their high specific power densities and specific energy densities compared to rechargeable batteries and traditional dielectric capacitors, respectively.[1,2] Over the last three decades, research on supercapacitors has increased exponentially, different materials and synthesis techniques are being employed for supercapacitive materials.[3–5] The prime focus of supercapacitive materials are carbon derivatives,[6] metal oxides,[7] chalcogenides,[8] and conducting polymers.[9] In addition to the above conventional materials, new materials, such as transition metal carbides[10] and phosphides,[11] are being explored. Recently, researchers have been focused on high entropy alloys (HEAs) for applications, such as energy storage and conversion,[12] electrocatalysis,[13] gas sensing, and storage,[14] proving their outstanding physicochemical properties. In addition, transition metal high entropy alloys (TMHEAs) have been one of the evolving electrode materials for supercapacitors, exhibiting promising capacitive performance.[15,16] Also, a few two-dimensional (2D) materials have been explored in the field of supercapacitors,[17] such as metal–organic frameworks,[18] nickel-based materials,[19] 2D copper-based materials,[20] cobalt–nickel–tungsten nanosheets,[21] and 2D cobalt-based materials.[22,23] TMHEAs are formed by mixing various metallic elements and have specific physicochemical characteristics, such as outstanding magnetic and electrical properties, and high thermomechanical stability when the size is decreased to nanometer range.[24,25] Also, TMHEAs exhibit more redox active sites, and their three-dimensional diffusion channels aid towards the easy flow of the electrolyte,[16] almost ending the limitations of poor cycling stability and material degradation during electrochemical tests. In this regard, various TMHEAs and their oxides have been studied with different morphologies, such as nanoporous,[26] quasi spherical,[27] and nano agglomerations,[28] along with some HEA composites, such as rHEA-CNT,[29] MnO_2–FeCrCoMnNiAl$_{0.75}$,[30] and HEA-nitrides,[31] for supercapacitor applications.

Among these TMHEAs, CoCrNiFeMn (CCNFM) HEA is being explored in the field of supercapacitors. Also, CCNFM exists in the stable crystalline phase, FCC structure[32] irrespective of synthesis techniques. Recently, several techniques, such as liquid phase synthesis,[33] solid phase synthesis methods,[34]

[a] *School of Nano Science and Technology, Indian Institute of Technology, Kharagpur, West Bengal-721302, India. E-mail: k_biswas@metal.iitkgp.ac.in, chandra.tiwary@metal.iitkgp.ac.in*
[b] *Materials Research Centre, Indian Institute of Science, Bengaluru – 560012, India. E-mail: abhishek@iisc.ac.in*
[c] *Department of Metallurgical and Materials Engineering, Indian Institute of Technology, Kharagpur, West Bengal-721302, India*
[d] *Department of Materials Engineering, Indian Institute of Technology-Jammu, Jagti, Jammu-181221, India*

† Electronic supplementary information (ESI) available. See DOI: https://doi.org/10.1039/d3ma00327b

and gaseous phase[35] synthesis, are being adopted to produce TMHEAs. There is also a demand to develop a stable nanostructured HEA porous material for electrochemical applications. Moreover, CCNFM also possesses higher electrical, mechanical, and specific surface properties, which are effective in electrochemical analysis.[36,37]

Here, we report CCNFM nanoparticles synthesized by a simple, scalable induction melting followed by a ball milling process and explored its potential in device-grade supercapacitor applications. At first, the three-electrode study was carried out for optimized concentration of KOH aqueous electrolyte. Herein we obtained a maximum specific capacitance of 386.66 F g^{-1} at 5 mV s^{-1} for 3 M potassium hydroxide (KOH). Consequently, a liquid state CCNFM HEA//AC asymmetric device was fabricated in a 3M KOH aqueous electrolyte. The device's energy and power density were 21 W h kg^{-1} and 307 W kg^{-1}, respectively. We studied the d-band centres of individual metals contributing electrons near the Fermi level to facilitate the overall charge transfer in the system by means of DFT studies. We also discuss post-electrochemical FESEM analysis and post-XPS in order to understand the detailed mechanism of charge storage in CCNFM. The liquid state device's performance was also compared with various ASC liquid state devices as well as HEA-based supercapacitive materials.

Material and methods

Synthesis of CoCrNiFeMn HEA

Nickel, chromium, cobalt, manganese, and iron metals were purchased from Loba Chemicals, India (99.99%) and used without further purification. Potassium hydroxide (KOH), activated charcoal, and polyvinylidene fluoride (PVDF) powders were obtained from Merck India.

The synthesis of CCNFM was carried out using a sealed induction melting process.[23] In this process, an equimolar mixture (0.2 molar) of cobalt, chromium–nickel, iron, and manganese were sealed in an argon atmosphere followed by induction melting at 1350 °C. To ensure chemical homogeneity, the cast ingot was melted three to four times and solidified. For homogenization, the cast HEA bulk was sealed in a quartz tube at vacuum conditions, heat treated at 1000 °C for 96 hours, and then followed by furnace cooling. After ensuring the single-phase formation, the ingot was parted into smaller pieces and vibratory high-energy ball milling for 16 hours to form HEA nanomaterial.

Characterization

X-ray diffraction (XRD) study was executed on CCNFM HEA bulk using Cu Kα radiation (λ = 1.5406 Å) on the D8 Advance Brukers diffractometer, Germany. FESEM (Zeiss supra-40) was used to determine the particle distribution morphologies of the CCNFM HEA powders. Additional morphological analysis was performed using a transmission electron microscope with an operating potential of 200 kV (JEM 2100, JEOL Ltd, Tokyo, Japan). Further X-ray photoelectron spectroscopy (XPS) measurements were performed on the HEA nanoparticles using the XPS Microprobe (PHI Versa Probe III) with Al Kα source (1486.7 eV). Furthermore, the multipoint BET surface area was measured using the Quantachrome Nova 1000 instrument. Average particle size and zeta potential were measured using Litesizer 500, model BM 10.

Electrochemical study

Electrochemical studies on CCNFM electrodes were conducted using the Biologic E (SP 200, France) instrument. All electrochemical measurements were performed in a three-electrode arrangement in a 3 M KOH aqueous electrolyte. The desired electrodes were used as an active material coated on a graphite sheet (working), saturated calomel electrode (reference), and platinum wire (counter). The obtained nanomaterial was used as a working electrode in three-electrode measurements. To construct a working electrode, a slurry was prepared with 70 wt% of capacitive material (CCNFM powders), 20 wt% of carbon black as a conducting reagent, and 10 wt% of PVDF as a binding reagent, in which 1-methyl-2-pyrrolidone (NMP) was added to the above mixture to make a homogeneous slurry and ground with mortar pestle, followed by ultrasonication for 30 min. Then, the slurry was coated on a 1 cm^2 graphite sheet (1 × 2 cm^2 size, 0.2 mm thick, Sigma Aldrich) and vacuum dried for 8 h at 60 °C. Before drop casting, the graphite sheet was cleaned with acetone. The mass loading on the working electrode was kept at 1 mg of capacitive material.

The specific capacitance (C_S) was calculated from a cyclic voltammogram using eqn (1)[38]

$$C_s(\mathrm{F\ g^{-1}}) = \frac{\int_{V_i}^{V_f} I(V)\mathrm{d}V}{m\nu(V_i - V_f)} \quad (1)$$

where, I, $\int_{V_i}^{V_f} I(V)\mathrm{d}V$, $(V_i–V_f)$, m and ν represent the discharge current density (A g^{-1}), area of cyclic voltammetry, stable potential window, mass loaded on graphite sheet, and scanning rate, respectively.

Since CCNFM exhibits nonlinear charge–discharge curves (pseudocapacitance mechanism), C_S was calculated using eqn (2)[39]

$$C_s(\mathrm{F\ g^{-1}}) = \frac{I\int V\mathrm{d}t}{m(V_i - V_f)^2} \quad (2)$$

here, $\int V\mathrm{d}t$ is the area under the galvanostatic discharge curve.

Computational methodology

To gain further insights, first-principles calculations were performed using density functional theory (DFT) as implemented in the Vienna *ab initio* simulation package (VASP).[40] The electron–ion interactions were described using all-electron projector augmented wave (PAW) pseudopotentials[41] and the electron exchange and correlations were approximated using Perdew–Burke–Ernzerhof (PBE) generalized gradient approximation (GGA).[42] 13-atom icosahedron nanoclusters of Co, Cr, Ni, Fe, and Mn were constructed using the atomic simulation environment (ASE) toolkit.[43] To construct

the 13-atom CoCrNiFeMn HEA nanocluster, d-band centre analysis was performed to choose the atoms in the ratio 3 : 3 : 3 : 2 : 2. A vacuum layer of 10 Å was applied in all three directions to prevent spurious interaction between periodic images. The Brillouin zone was sampled at the Γ point for relaxation of nanoclusters, however, for density of states (DOS) calculations, a 4 × 4 × 4 Monkhorst–Pack grid was deployed. An energy cut-off of 450 eV was used for selecting the plane-waves. The 13-atom nanoclusters were fully relaxed using a conjugate gradient scheme until the energies and forces converged to 10^{-5} eV and 0.01 eV $Å^{-1}$, respectively.

Results and discussion

Structural and morphological analysis

Fig. 1(a) represents the schematic of synthesized nanostructured CCNFM HEA. The XRD pattern of CCNFM shows single FCC phase formation (Fig. 1(b)), which was also confirmed from the optical image of the bulk ingot (Fig. 1(c)). The XRD peaks occurring at 43.32°, 50.45°, and 74.12° correspond to (111), (200), and (220) planes of FCC crystalline structure, respectively.[44] The calculated value of the lattice constant for nanostructured HEA was a = 3.6 Å. The FESEM of the CCNFM agglomerated nanoparticles is represented in Fig. 1(d). It was observed that there was a large interface for the electrode/electrolyte interaction with the agglomerated nanoparticles to deliver multivalent redox sites to boost fast electron transport, which increases the pseudocapacitive performance.[45] In addition to morphological studies, energy dispersive X-ray spectroscopy (EDS) of CCNFM powders was also carried out. The broad peaks in EDS indicated the purity of CCNFM with Co, Cr, Ni, Fe, and Mn elements in the atomic ratio of 11.30 : 25.94 : 13.71 : 32.12 : 16.93, respectively. Further elemental distribution (Fig. 1(e)) along with mapping (Fig. S1, ESI†) showed the uniform distribution of elements, as mentioned

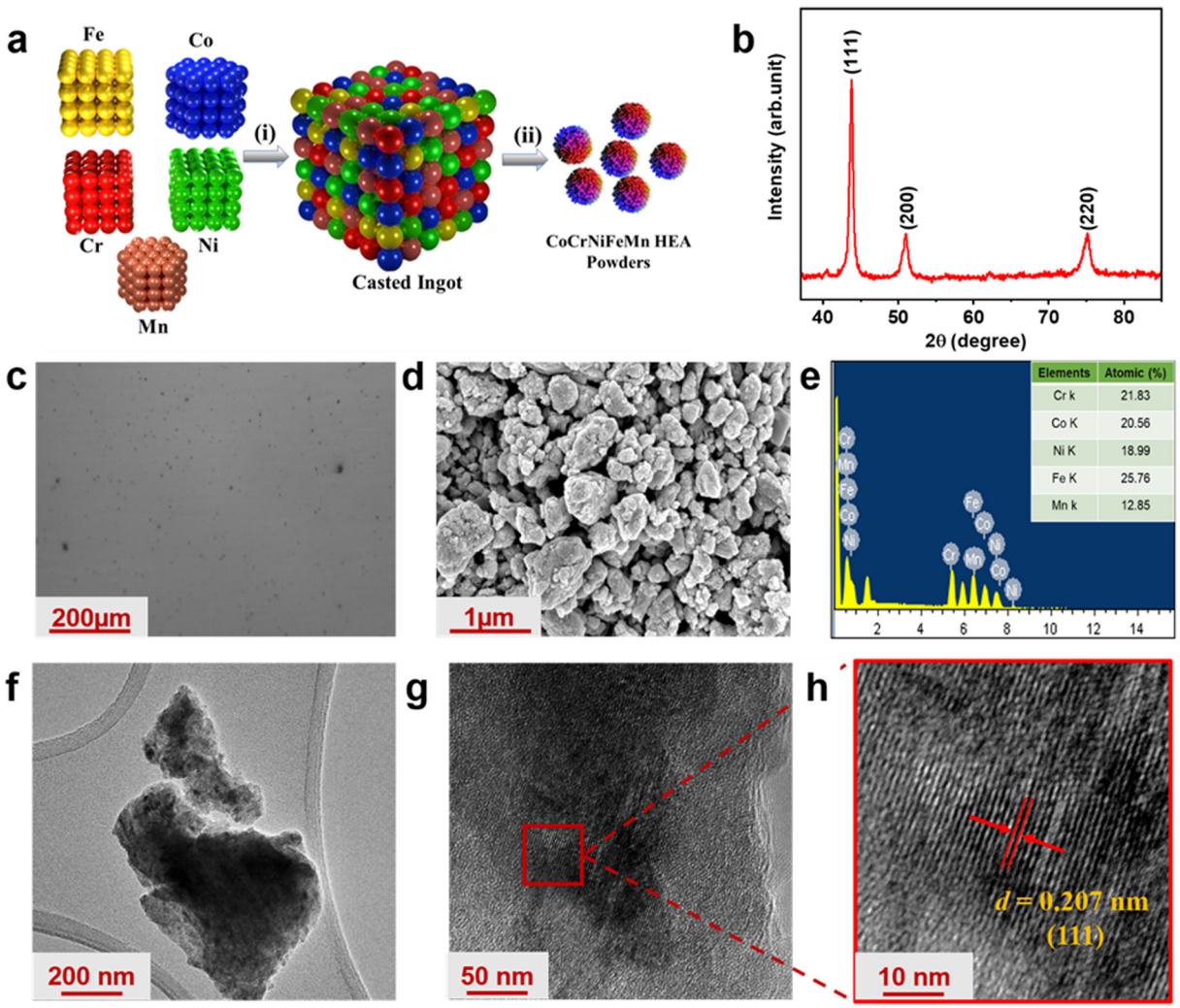

Fig. 1 (a) Schematic illustration of the synthesis of the quinary CCNFM HEA material (i) after induction melting and heat treatment and (ii) after high-energy ball milling. (b) XRD pattern of the CCNFM HEA powder. (c) Optical image of CCNFM HEA bulk. (d) FESEM image of CCNFM HEA powder. (e) EDAX spectrum of the same. (f) HAADF STEM image of the agglomerated structure. (g) HAADF-STEM image showing multiple planes and (h) single plane mapped with a d spacing of 0.207 nm.

earlier. High-angle annular dark-field scanning transmission electron microscopy (HAADF-STEM) was obtained for the ball-milled sample in Fig. 1(f–h). A thin section of the agglomerated HEA sample is shown in Fig. 1(f). The planes are evident in Fig. 1(g); a single plane was further processed (Fig. 1(h)), which shows lattice fringes with a d spacing of 0.207 corresponding to the (111) plane.[46]

Further compositional analysis of CCNFM was performed using X-ray photoelectron spectroscopy (XPS). The XPS survey clearly shows the presence of Cr, Co, Ni, Fe, and Mn, which are the primary elements in HEA, as represented in Fig. 2(a). The appearance of the broad oxygen peaks is due to the surface oxidation of the quinary elements.[47] The peaks agreed with those for $Co2p_{3/2}$ and $Co2p_{1/2}$ at 780.62 eV and 796.51 eV, respectively, and were allocated to Co^{2+},[48] and the peaks at 785.5 eV and 802.33 eV are allocated to the two satellite peaks. Fig. 2(c) shows an effect of spin–orbit splitting $2p_{3/2}$ and $2p_{1/2}$ energy states at 576.29 and 586.28 eV, respectively for Cr^{3+} with an energy splitting of 10 eV.[27,28] The satellite peak appearing at 578.41 eV shows the occurrence of mixed valence states. Fig. 2(d) shows XPS spectra of Ni 2p core energy states. Splitting of $2p_{3/2}$ and $2p_{1/2}$ energy states appear at 855.43 and 872.78 eV, respectively, and it belongs to Ni^{2+}.[49] The satellite peaks appearing at 861.48 and 879.78 eV direct the mixed valence states. In the Fe2p spectrum, as shown in Fig. 2(e). The broad peaks at 710.73 eV and 724.19 eV correspond to $Fe2p_{3/2}$ and $Fe2p_{1/2}$, respectively, of Fe^{3+}. The energy difference between the broad two peaks was 13.46 eV, confirmatory of the formation of Fe_2O_3 on the surface.[50] The peaks at 713.75 and 717.05 eV belong to Fe^{2+} and satellite peaks, respectively. Mn's XPS spectra are shown in Fig. 2(f). The 2P energy splitting $2p_{3/2}$ and $2p_{1/2}$ energy states are seen at 641.17 and 653.01 eV and they belong to Mn^{3+} of Mn,[51] respectively, and energy splitting of 11.84 eV. Further the peak at 644.37 eV refers to the satellite peak of Mn.

Along with the phase and morphological analysis, the particle size and zeta potential also play an important role in the performance of an electrode material.[52] The particle size distribution obtained from dynamic light scattering (DLS) data and averaged particle diameter was ~500 nm for CCNFM ball-milled samples, as shown in Fig. S2 (ESI†). Uniform particle size distribution was observed, which proves the suitability of the synthesis protocol to produce products with uniform size over wide size distribution. The particle size is tuneable, and is controlled *via* the ball milling process. The average particle diameter was kept at the submicron level in order to improve its ease of ion interaction in the electrolyte during electrochemical measurements. The particle size reduction also paves the way for more surface-active sites in the powder sample. Fig. S4a (ESI†) shows the zeta potential for the CCNFM HEA powder as 24.48 mV. This indicates good physical stability of nanoparticles due to the electrostatic forces of distinct particles and accumulation of particles, which was also clearly visible in the FESEM image. The surface area to volume ratio for a nano range of materials with excellent pore size dispensation plays an important role in determining specific capacitance.[53] In that aspect, the effective BET surface area of nanostructured CCNFM is crucial. The distribution of pore volume over pore size was estimated using the BJH model. The nitrogen adsorption and desorption isotherms of CCNFM (Fig. S4b, ESI†) follow a classic Type-IV trait. This forms a hysteresis loop in the range of 0.1 to 1.0 of relative pressure (P/P_0). The BET surface area was calculated to be 25 $m^2\ g^{-1}$. Also, from the pore size distribution it was observed that the maximum of the pores belongs to the mesoporous region, as shown in Fig. S4c (ESI†). The resulting effective surface area offers electro active sites to improve electrochemical performance.

Fig. S3a (ESI†) shows the Tauc plot derived from UV-visible spectroscopy of the ball-milled HEA powder with a bandgap of 1.26 eV. HEA bulk being an alloy has E_g = 0, when the dimension was reduced to a submicron level, a bandgap opening was observed. This is a common aspect arising due to structural change in the material.[54] Raman spectroscopy was also performed (Fig. S3b, ESI†) for the ball-milled HEA powder. Major peaks were observed at 136, 300, 410, 519, 590, and 660 cm^{-1}. The peaks correspond to $3F_{2g}$, A_{1g} (LO), and E_g (TO) modes of chromites, ferrites, aluminites, and spinels.[55,56] These peaks show the evident surface oxidation formation pertaining to each of the five elements in the CCNFM HEA. This offers valence states (also seen in XPS, Fig. 2(a–f), in turn assisting the electrochemical performance of the electrode. Therefore, making metal oxides Fe–O, Ni–O, Co–O, Cr–O, and Mn–O as the epicentre of electrochemical activities in CCNFM HEA agglomerated nanostructures.

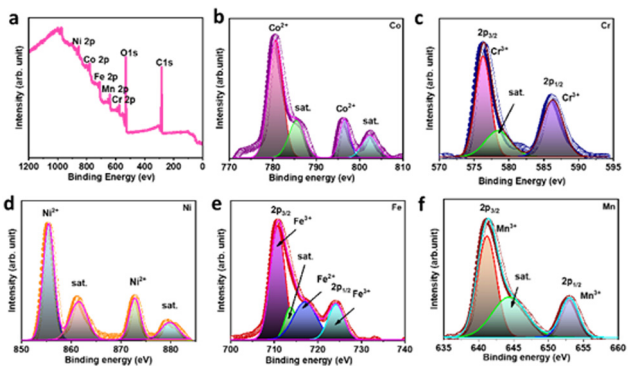

Fig. 2 XPS survey profile of CCNFM HEA powder (a) before electrochemical measurements. XPS spectra of individual elements of Co 2p (b), Cr 2p (c), Ni 2p (d), Fe 2p €, and Mn 2p (f).

Electrochemical analysis

In a 3 M KOH aqueous electrolyte, the working CCNFM HEA electrode was optimized in the voltage region of −0.1 to 0.5 V against the reference Ag/AgCl electrode for further measurements. The selection of the aqueous KOH electrolyte is due to the fact that at room temperature, K^+ ions exhibit a molar ionic conductivity of 0.00735 S m^2 mol^{-1} facilitating rapid charge transfers, allowing for enlarged ion adsorption at the electrolyte/electrode boundary, boosting the electrochemical performance.[57] The multivalent elements in the CCNFM results

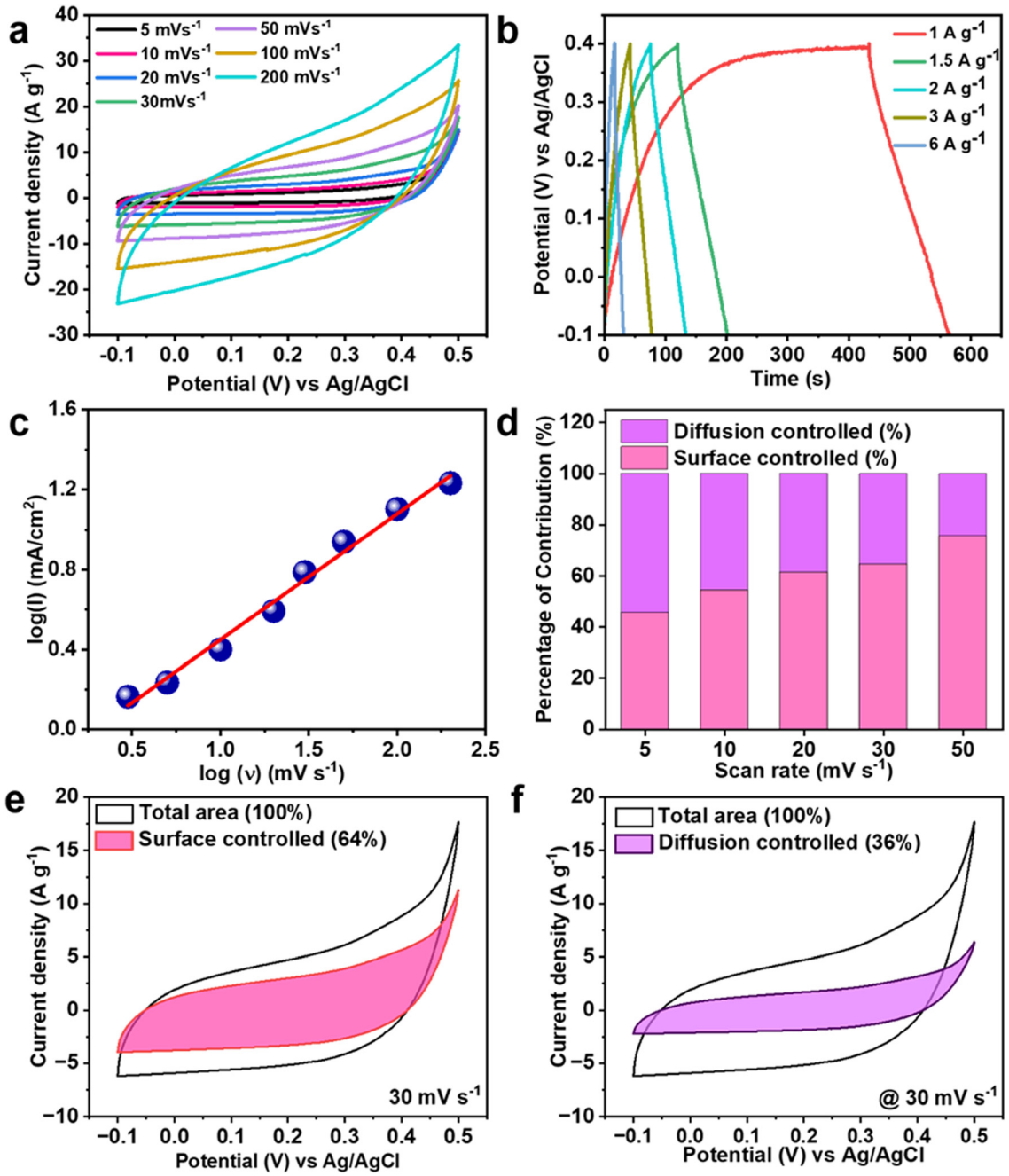

Fig. 3 (a) Cyclic voltammograms of the CCNFM HEA electrode at 3M KOH. (b) GCD curves. (c) Plot for *b* value log I (A) *vs.* log ν (mV s^{-1}). (d) Charge contribution profiles at different scan rates. (e) and (f) The diffusion-controlled faradaic and surface-capacitive currents are separated from the total current at 30 mV s^{-1}.

in more redox pivots for collecting the K^+ ions. The CV curves from 5 mV s^{-1} to 200 mV s^{-1} are shown in Fig. 3(a), there was no clear appearance of reduction and oxidation peaks, suggesting that the HEA electrode not only possesses pseudocapacitance but also has capacitor-like properties.[58] The peak redox potential shifts only slightly within the sample, while the current increases significantly with an increasing sampling rate as theoretically predicted by researchers.[59,60] Such scanning rate performance and high cyclic area under the CV curves are because of the inductive effect of the highly conducting quinary metal elements and oxide surface of the core and active surface in the electrolyte. In the negative potential window, iron and chromium undergo redox reaction[61,62] while cobalt and nickel[63,64] further contribute to CV in the positive potential window as important pseudo-capacitive materials (*viz.* Fe, Co, Ni) allowing more electron transport. In addition to CVs, galvanostatic charge–discharge (GCD) was performed for the CCNFM electrode within the potential windows of 0.4 to −1.0 V

in 3 M KOH aqueous solution, Fig. 3(b). When different GCD plots are taken into consideration at 1, 1.5, 2, 3, and 6 A g^{-1}, neither pure triangular nor pure plateau shapes are observed, which indicates that the contribution is not purely faradaic but there is also capacitive-type behaviour. Also, from Fig. 3(b) it can be noted that this CCNFM HEA electrode shows moderate coulombic efficiency, due to parasitic redox reaction/degradation reaction associated with surface oxidized multielement HEA. The coulombic efficiency can be improved with the help of chemical treatment or combining with another material.

The specific capacitance calculated from the CV curve using eqn 1 was around 386.66 F g^{-1} at 5 mV s^{-1} with increasing scan rate by 40 times the capacitance drops to 105.22 F g^{-1} at 200 mV s^{-1}. The specific capacitance for the CCNFM electrode was evaluated from the discharge time of the GCD curve using eqn 2. The highest specific capacitance obtained was ~264 F g^{-1}, at 1 A g^{-1}, and 64.39% capacity retention occurred when the current density was increased six times. This proves practical rate competence and better pseudocapacitive phenomena of the HEA electrode, which is supposedly promoted by the facile electron carriage over its multivalent quinary mesoporous architecture. Additionally, the CCNFM offers abundant multivalent active redox sites for additional electrolyte ions to be accessed.

Any supercapacitive electrode stores charge using two main processes, namely surface capacitive and diffusion control.[65] The surface capacitive charge storage mechanism is commonly known as the electrochemical double-layer capacitance (EDLC), which arises from the accumulation of electrolytic ions on the surface of the electrodes. While a slow diffusion-controlled mechanism stands with the bulk faradaic charge storage mechanism in the form of ion intercalation activities. With the purpose of quantifying the exact contribution of the above two processes, we use power law[66],[67] followed in eqn 3,

$$I = a\nu^{b} \tag{3}$$

where I is current and ν is the scan rate, a and b are modifiable parameters for the above relation. The value of b ranges from 1 to 0.5, where 0.5 signifies pure faradaic storage mechanism, while 1 refers to pure EDLC dominance with rectangular CV format. The exact value of b is determined at a potential 0.1 V point, which is 0.66, as shown in Fig. 3(c), and is close to the highly localized fast faradaic charge storage and slow diffusion-controlled process through redox reaction occurrences.[68] Therefore, CCNFM has intrinsic pseudocapacitance significant to their nano agglomeration architecture helping reduce the ion diffusion path, expanding when there is strong ion intercalation and de-intercalation of electrolytic ions.[69]

In an electrochemical process, the amount of charge $Q(t)$ can be quantified as surface controlled Q_s and diffusion controlled Q_d[70] as termed in eqn (4)

$$Q(t) = Q_S + Q_d \tag{4}$$

The surface-controlled total charge can be evaluated from the relation $Q(\nu)$ and $\nu^{-\frac{1}{2}}$, which is found at the intercept of the x-axis, as shown in Fig. S3 (ESI†).

$$Q(\nu) = Q_S + Q_d = Q_{\text{capacitive}} + k_3\nu^{-\frac{1}{2}} \tag{5}$$

The separate contribution of the surface controlled (Q_s and diffusion controlled (Q_d) at various scan rates is plotted in Fig. 3(d), which show the predominance of diffusion-controlled processes over the surface-controlled one. This represents CCNFM of having more faradaic redox active sites with porous structures proving to participate in the entire slow diffusion-controlled process in a lower scanning rate (more time period available for interaction) while increasing the scanning rate the ions do not have sufficient time to participate at the diffusion-controlled process, so thereby dominance of surface-controlled reactions. By considering a particular scan rate of 30 mV s^{-1}, each contribution of Q_s and Q_d is shown in Fig. 3(e) and (f). In the CCNFM HEA nanoparticles, the charge storage characteristics originated from the surface oxidation of multivalent quinary elements. This mechanism can be clearly described as interaction with aqueous KOH electrolyte and can be explained with surface oxides of individual quinary elements,[71,72] such as:

$$NiO + OH^- \Leftrightarrow NiOOH + e^-$$

$$CoO_2 + H_2O + e^- \Leftrightarrow CoOOH + OH^-$$

$$MnO_2 + K^+ + e^- \Leftrightarrow MnOOK$$

$$Fe_3O_4 + 2OH^- \rightarrow 3\ Fe(OH)_2 + 2e^-$$

$$3Fe(OH)_2 + 2OH^- \rightarrow Fe_3O_4 + 4H_2O + 2e^-$$

$$CrO(OH) + OH^- \rightarrow CrO(OH)_3 + e^-$$

Again, these surface oxidized quinary metals display variable oxidation states, which back faradaic interaction with the KOH electrolyte. During these redox activities, changes in the oxidation state from M^0 to M^{+2} and further M^{+2} to M^{+4}/M^{+3} and vice versa[27] are well explained in the post-XPS section Fig. 7(ii)(a–f).

The cyclic stability of the three-electrode system was studied in a 3M KOH electrolyte at a scan rate of 200 mV s^{-1} up to 5000 cycles, as shown in Fig. 4(a). The initial capacity decays around 98% for the first 1000 cycles, while when it reaches 3000 cycles, the stable capacity retention was around 96%. It is clear after 5000 cycles that the capacity retention was 96% of the initial specific capacitance. This extraordinary cyclic performance is believed to have originated from the surface oxidation quinary HEA system interaction with an aqueous KOH electrolyte. The initial and final CVs of 200 mV s^{-1} are shown in insert Fig. 4(a). In addition to the cyclic voltammograms (CV) and galvanostatic charge–discharge (GCD), electrochemical impedance spectroscopy (EIS) was performed in the frequency range between 10 kHz to 1 Hz. The Nyquist plot is shown in Fig. 4(b) along with the fitted circuit. The circuit contained simple total internal resistance (R_s), and a constant phase eliminator (CPE). The value of R_s was found to be 2.08 Ω cm^{-2} from the intercept of the real impedance axis. The possible reason for the

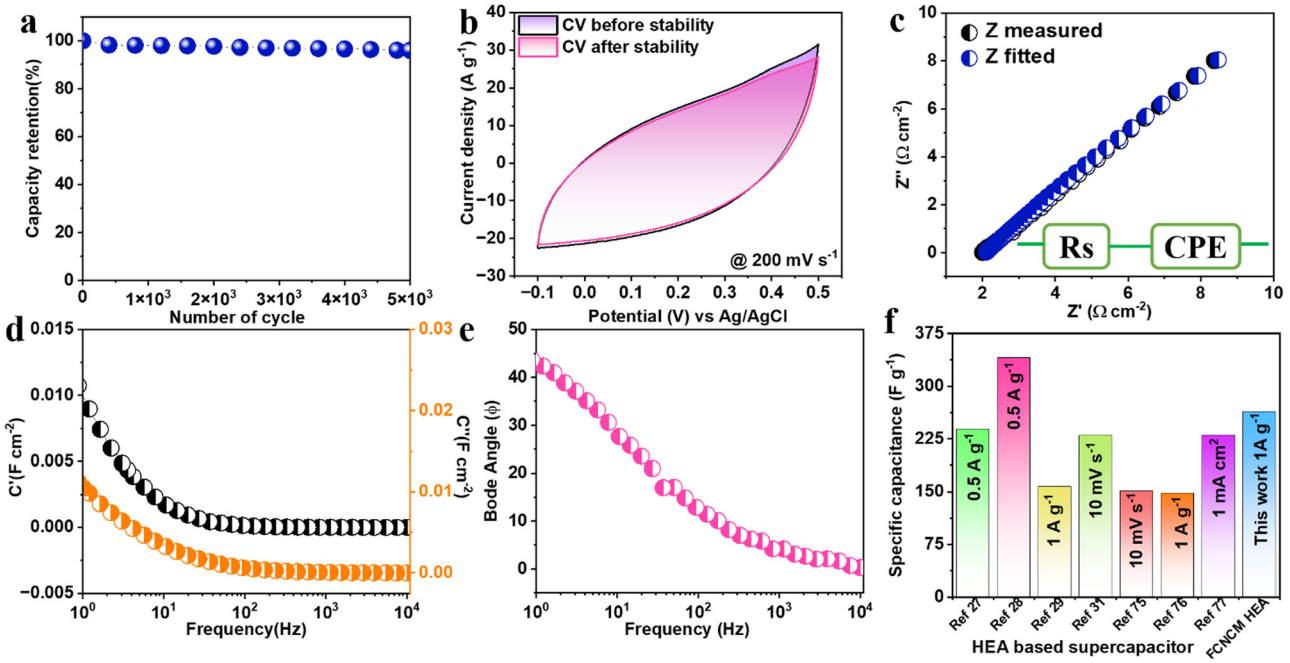

Fig. 4 (a) Cyclic stability of CCNFM HEA electrode (b) CV before and after 5000 cycles at 200 mV s^{-1}, (c) Nyquist plot for the three-electrode CCNFM HEA system (d) capacitance components *vs.* frequency (e) phase angle *vs.* frequency (bode plot) (f) comparison plot for specific capacitance on HEA based supercapacitor.

appearance of the constant phase eliminator may be due to the surface roughness of the electrode, non-uniform current distribution, and distribution reaction rates.[73] The constant phase eliminator is inclined in nature. The fitted circuit shows perfectly polarized capacitive-like behavior. The frequency-dependent capacitive components were further calculated using eqn 12 and 13. The real capacitive (C') and imaginary component (C'') along with frequency are shown in Fig. 4(c). Where C'' refers to the energy dissipation caused by the uncomplimentary irreversible process (resistive loss) and C' refers to the accessible capacitance component. Furthermore, the current quality response analyzed using a bode plot, Fig. 4(d) shows the phase angle as a function of frequency. The ideal phase angle for the perfectly capacitive component is 90°. In this electrode material testing, the phase angle is close to 55°, which more consequently explains the capacitive behavior of the electrode. In a comparison with various HEA-based supercapacitors in this work, CCNFM HEA exhibits higher specific capacitance around 264 F g^{-1} at 1 A g^{-1}, as shown in Fig. 4(e) Various HEA-based materials, such as $(CrMnFeCoNi)_3O_4$,[27] $(FeCoCrMnZn)_3O_4$,[28] HEA-Nitrides[31] $(FeCoCrMnNi)_3O_4$[74] exhibits specific capacitance of 239 F g^{-1}, 340.3 F g^{-1} at the current density of 0.5 A g^{-1}, 230 F g^{-1} at 10 mV s^{-1} and 332.2 F g^{-1} at 0.3 A g^{-1}, respectively. While some HEA-based composites such as rHEA-CNT,[29] (VNbTaZrHf)C,[75] HEO/f-CSAC,[76] and FeNiCoMnMg HEA-NPs/ACNFs[77] show specific capacitance of 157.5 F g^{-1} at 1 A g^{-1}, 151 F g^{-1} at 10 mV s^{-1}, 147.5 F g^{-1} at 1 A g^{-1} and 203 F g^{-1} at 1 mA cm^{-2}, respectively. We concur from the present work that CCNFM HEA can be an ideal competitor among HEA-based supercapacitive materials irrespective of the synthesis and composite combinations.

Devices studies

Asymmetric supercapacitor devices are better known for achieving high energy density as well as high power density. In this regard, mesoporous CCNFM was further employed for fabricating liquid-state asymmetric devices. For this purpose, positive and negative electrodes were fabricated using CCNFM and AC, respectively. In order to understand the mass loading, the corresponding CV (the three-electrode system) of AC and HEA with potential windows −1.0 to 0.0 V and −0.1 to 0.5 V at 50 mV s^{-1} sweep rate, respectively, are shown in Fig. 5(a). From both potential windows, the CCNFM//AC device can be operated up to 1.5 V without any CV disintegration.

To achieve maximum device performance, charge-balanced mass loading was performed with the assistance of charge balance theory[78] using eqn (6)

$$Q^+ = Q^-/V^+ \quad (6)$$

$$\frac{m_+}{m_-} = \frac{C_{s-}\Delta V_-}{C_{s+}\Delta V_+} \quad (7)$$

where m_+ and m_- are mass loadings, C_{s-} (95.66 F g^{-1}) and C_{s+} (233.33 F g^{-1}) of the negative (AC) and positive HEA at 50 mV s^{-1}, with ΔV_- (1V) and ΔV_+ (0.6 V) potential window AC and CCNFM HEA, respectively. After substituting the respective values, the ratio obtained was 0.67. Therefore, 1 mg of HEA powders and 1.5 mg of activated carbon were used to prepare the electrodes for the ASC device. Furthermore, the electrode preparation was similar to that of a three-electrode system. For the negative electrode, AC: carbon black and PVDF (70 : 20 : 10) with 1 mL of NMP slurry was prepared and coated on a graphite sheet (1 cm^2). Next, a device study was performed using the 3 M

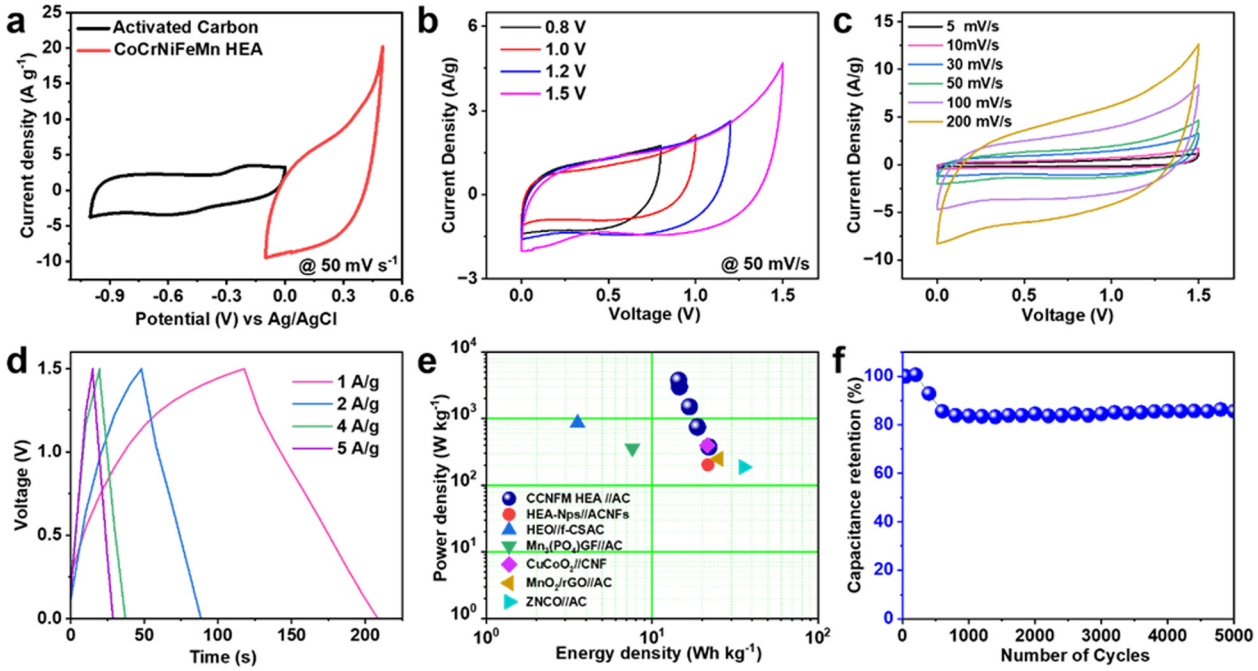

Fig. 5 (a) CV curve of AC and CCNFM HEA at 50 mV s^{-1}. (b) CV profile of ASC device at different potential windows. (c) CV scans for ASC device. (d) GCD plot. (e) Ragone plot. (f) Capacity retention.

KOH electrolyte. Fig. 5(b) shows CV stability at 50 mV s^{-1} with diverse potential windows ranging from 0.8 to 1.5 V. In the stable potential 1.5 V, the CV scans were taken between 5 mV s^{-1} to 200 mV s^{-1}, as shown in Fig. 5(c). The behavior of curves is quasi-rectangular, with no sign of any electrolyte disintegration. Thus, the device can work up to 1.5 V. Specific capacitance values for the ASC device evaluated from CV curves with the help of eqn 1 were 104.85 and 44.85 F g^{-1} at scan rates of 5 and 200 mV s^{-1}. Furthermore, from the GCD plot taken at current density 1 A g^{-1} to 5 A g^{-1}, as shown in Fig. 5(d), the specific capacitance was evaluated using eqn (2), and 60.05 F g^{-1} at a current density of 1 A g^{-1} was obtained. With increasing current density value to 5 A g^{-1}, the value of capacity retention drops to 78.61%, which is considerably good even at a higher current rate of up to 5000 cycles at 5 A g^{-1}.

Further, the energy density and power density were evaluated for the ASC device using eqn (8) and (9).[79,80]

$$E = \frac{I \int V \mathrm{d}t}{m} \tag{8}$$

$$P(\mathrm{W\,kg^{-1}}) = \frac{E}{\Delta t} \tag{9}$$

Where, I refer to current density, $\int V \mathrm{d}t$ is the integral area under the discharge curve, m is mass loading, Δt is the discharge time.

The energy density values were 21 (at 0.5 A g^{-1} as shown in Fig. S4, ESI†), 18.85, 16.83, 14.616, and 14.45 W h kg^{-1} at power densities of 0.3, 0.75, 1.5, 3, and 3.75 kW kg^{-1}, respectively. As shown in the Ragone plot in Fig. 5(e), the ASC device shows a clear understanding of excellent supercapacitive properties. Among high entropy-based supercapacitive materials, FeNiCoMnMg HEA-NPsACNFs[77] and HEO/f-CSAC[76] showed 21.7 and 3.55 W h kg^{-1}, respectively, compared to our ASC device that showed 21 W h Kg^{-1}. Among other asymmetric liquid state devices, Mn_3PO_4 GF//AC,[81] $CuCoO_2$//CNF,[82] MnO_2-rGO//AC,[83] and ZNCO//AC[84] showed specific energy values of 7.6, 21.5, 25.14, and 35.6 W h kg^{-1} at a specific power of 360, 400, 250, 187.6, and 262 W kg^{-1}, respectively, as presented in Ragone plot. Although the above shows higher energy density at lower power density this CCNFM-HEA//AC performance is comparable with respect to low-cost synthesis and surface oxidized characteristics of quinary element. This is further improved with forming high entropy oxide. We have compared a few existing device specifications with our work shown in Table S1 (ESI†).

In order to understand the long-term stability of the CCNFM//AC liquid state device, cyclic stability was demonstrated up to 5000 GCD cycles taken at a current density of 5 A g^{-1}. The capacity retention along with GCD cycles is shown in Fig. 5(f) calculated using eqn 10. During the first 200 cycles, it was observed that there was no decrease in capacitive retention. While going towards the 5000 cycles, it was noted that the capacitance retention value reached 88.5%.

$$\text{Capacitance retention}(\%) = \frac{C_1}{C_n} \times 100 \tag{10}$$

C_1 and C_n are the specific capacitance at the first and nth cycles, respectively.

The electrochemical performance is mediated through the surface oxygen sites formed during the ball milling of

samples (Fig. 2a–f). The vacancy sites are evident from XPS measurements. Fig. 6 shows a schematic representation of the electrode–electrolyte diffusion process in the asymmetric device. HEA was used as a cathode and activated carbon as an anode material for the opposite electrode. An EDLC layer was observed during the fast faradaic process that is taking place in the electrode–electrolyte interface, inside the asymmetric device. The current capacitive performance is comparable with individual metal nanoparticles or oxides due to the synergism of Co, Cr, Ni, Fe, and Mn quinary elemental HEA. Also, two characteristic effects that directly contribute to the pseudocapacitive performance of the HEA electrode are the ''cocktail effect'' and ''lattice distortion''. The ''cocktail effect'' refers to the vulnerability to chemisorption of quinary HEA in which elements jiggle over the surface. The lattice distortion effect directly alters the localized atomic spacing by changing compressive as well as tensile strains on atomic radii during ball milling.[85–87] We also performed d-band centre calculations (DFT) in order to study the contribution of electrons for supercapacitive interaction in the material, as discussed in the next section.

Moreover, the electrochemical performance was further analyzed using the Nyquist plot of imaginary and real impedance components in the frequency range between 5 kHz and 1 Hz, as shown in Fig. 7(i)(a). The circuit was fitted to an impedance plot as shown in the **inset**. The circuit contains a simple series resistance (R_s) connected with a constant phase eliminator (CPE). The value of R_s was evaluated from the x-axis intercept at around 1.66 Ω cm^{-2}. Furthermore, the rate of electrochemical performance was defined by the relaxation time constant (τ_0), which marks the boundary between resistive and capacitive activity. The bode plot in Fig. 7(i)(b) shows the relation between the corresponding phase angle *vs.* frequency. The known phase angle of an ideal electrochemical double-layer capacitor is 90° but for the pseudo-capacitive variation from the above ideal value.

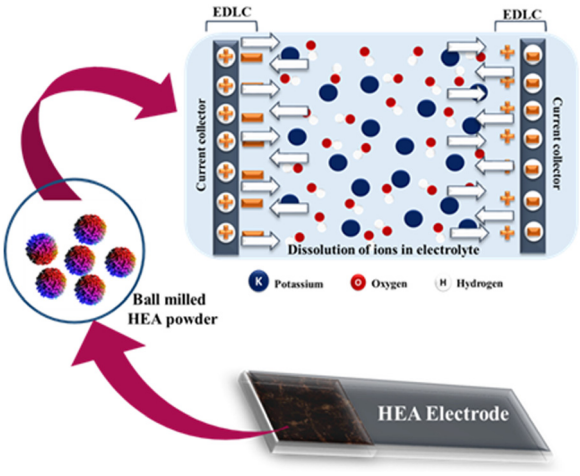

Fig. 6 Schematic representation of the electrode–electrolyte ion diffusion process in the asymmetric device.

The relaxation time can be calculated using eqn (11)

$$\tau_0 = \frac{1}{f_0} \tag{11}$$

The obtained τ_0 was 500 ms; this value of relaxation time constant signifies that moderate ion diffusion occurs at the electrode–electrolyte interface. The frequency-dependent imaginary (C'') and the real capacitive (C') parts are shown in Fig. 7(c). At the same time, C'' denotes the power dissipation resulting from the uncomplimentary irreversible technique (resistive loss), and C' is the reachable capacitance obtained on the corresponding frequency. The value of C'' can be calculated using eqn (12) and (13).[88]

$$C' = \frac{-Z''}{2\pi f |Z|^2} \tag{12}$$

$$C'' = \frac{Z'}{2\pi f |Z|^2} \tag{13}$$

With this, the above ASC device was used to glow a 1.5 V LED bulb as shown in Fig. 7(i)(d), depicting its practical use. FESEM images of HEA electrodes before and after 5000 cycles show no change in the original morphology, proving that the CCNFM electrode is highly stable even after repetitive charge–discharge cycles. The images show that there are pore openings at various spots, which are homogeneously distributed throughout the entire area of the electrode as shown in Fig. 7(i)(e) and (f). The material also seems to be stable and has not diffused majorly into the electrolyte during intercalation/deintercalation.

Further insight into the XPS electrode was obtained after 5000 cycles, as shown in Fig. 7(ii)(a–f). The increase in oxygen peaks and the presence of potassium peaks are clearly observed, suggesting the interaction with aqueous KOH electrolyte. Changes in the intensity of quinary cations suggest changing oxidation states during the redox activities of K^+ and OH^- ions. The variation of OH adsorption energy on Co, Cr, Ni, Fe, and Mn for 13-atom individual nanoclusters and CoCrNiFeMn HEA was theoretically calculated.

The adsorption energy was obtained using the following equation:

$$E_{ads}\,(OH) = E\,(OH + \text{nanocluster}) - E\,(\text{nanocluster}) - (E\,(H_2O) - 0.5 \times E\,(H_2)) \tag{14}$$

The maximum change in the adsorption energy was observed for Cr and the minimum for the case of Fe (Fig. S11, ESI†). We can also correlate the same from the XPS measurements that were performed before and after (5000 cycles) electrochemical measurements. Cr underwent a change in the valence states exhibiting multiple multivalent redox sites as compared to Fe element. These multivalent sites contribute to the electrochemical intercalation–deintercalation of ions on these sites.

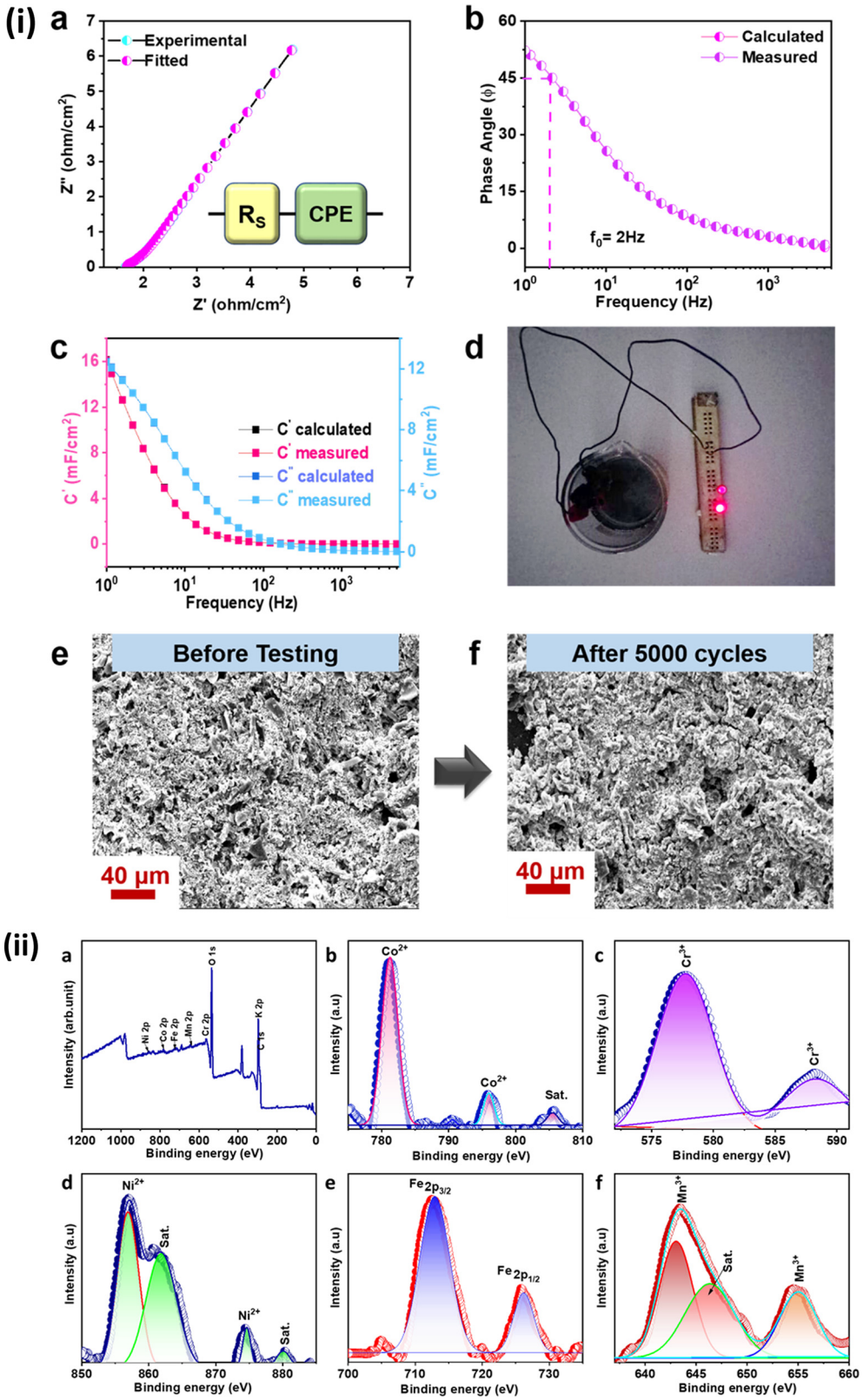

Fig. 7 (i) (a) Nyquist plot. (b) Bode plot. (c) Capacitance components *vs.* frequency plot. (d) ASC liquid state device is used to glow a 1.5 V led bulb. (e) and (f) FESEM images of CCNFM HEA electrode before and after 5000 cycles, respectively. (ii) XPS survey profile of CCNFM HEA powder (a) after 5000 cycles. XPS spectra of individual elements after 5000 cycles of Co 2p (b), Cr 2p (c), Ni 2p (d), Fe 2p (e), and Mn 2p (f), respectively.

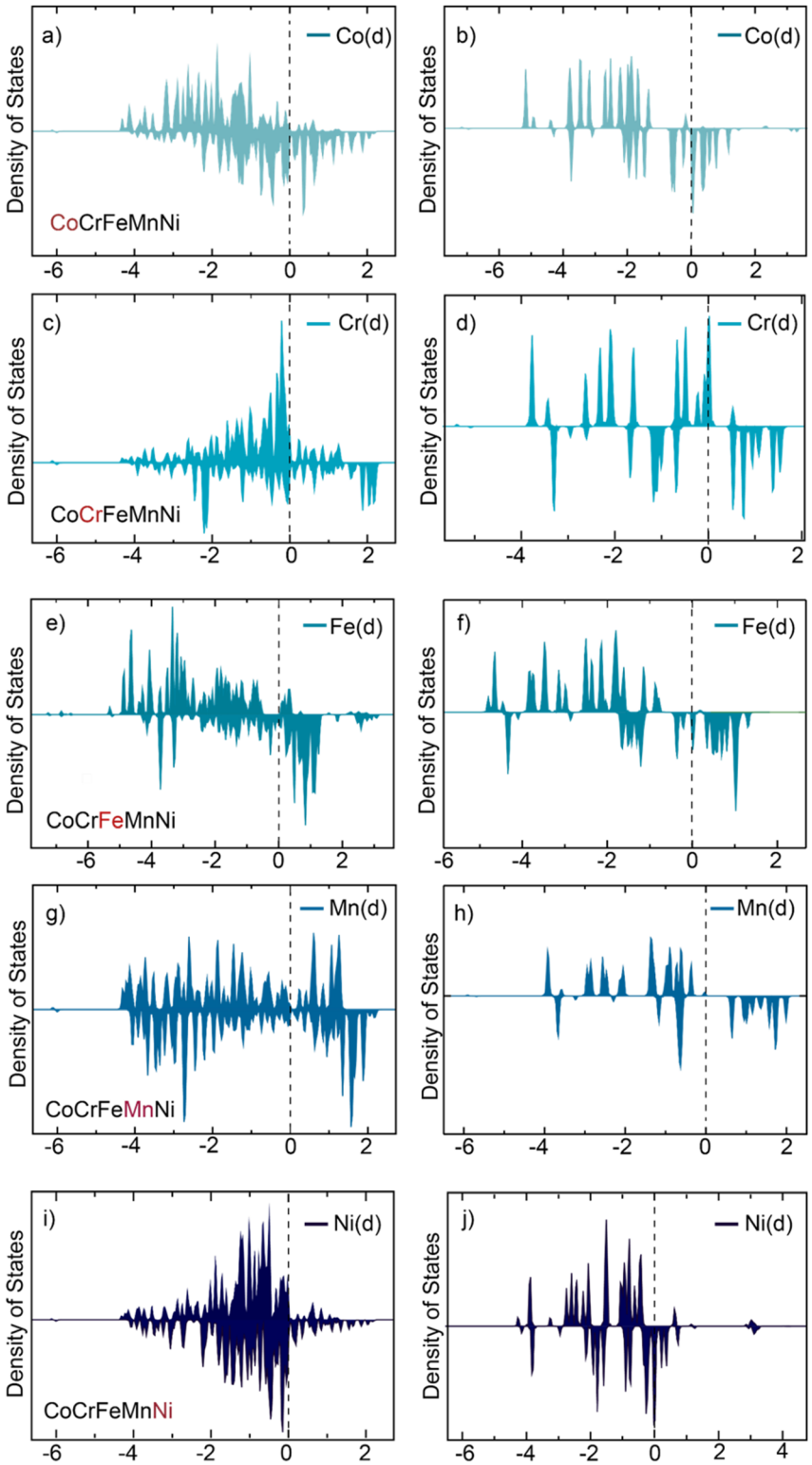

Fig. 8 Density of states plots for d-states of (a) Co, (c) Cr, (e) Fe, (g) Mn, and (i) Ni in CoCrFeNiMn HEA and the d-states for individual element 13-atom nanocluster of (b) Co, (d) Cr, (f) Fe, (h) Mn, and (j) Ni.

Theoretical studies

The position of the d-band centre with respect to the Fermi level provides information regarding the electron transferability of a metal.[89] When the d-band centre of a metal is near the Fermi level, the ability of a metal to accept or donate electrons increases, hence the electronic contribution of the metal increases. Here, to maintain the equimolar concentration, the d-band centre approach is adopted. The d-band centre analysis shows that the closeness of the

d-band of the individual atoms to the Fermi level follows the order Mn > Cr > Ni > Fe > Co (Fig. S10, ESI†), hence the concentrations of the individual atoms in the CoCrNiFeMn HEA nanocluster were taken as 3 : 3 : 3 : 2 : 2 corresponding to Mn:Cr:Ni:Fe:Co. Further, the density of states calculation confirmed that the d-states near the eFermi-level have significantly increased in random CoCrNiFeMn HEA compared to the individual atom nanoclusters (Fig. 8). The availability of the hybridised d-states near the Fermi level is attributed to the enhanced supercapacitance.[90] Maximum electronic redistribution was observed in the case of Ni and Cr below the Fermi level whereas Co and Fe had more hybridised d-states above the Fermi level, which indicated the contribution of the former to HOMO and later to LUMO.

From the above studies on the CCNFM HEA electrode, we show how a supercapacitor material with its multimetallic quinary framework helps to attain higher specific capacitance with the contribution of surface oxidation states and increased d-orbital electrons near the Fermi level in a High Entropy Alloy (HEA) system. Also, the detailed electrochemical study revealed that fast surface faradaic redox phenomena occurring at HEA interfaces boost intercalation/deintercalation. Furthermore, the liquid state asymmetric device demonstrated up to 1.5 V that was used to glow the LED bulb.

Conclusions

The scalable synthesis of CoCrNiFeMn HEA was successfully performed with the aid of induction melting, followed by vibratory high-energy ball milling. The required characterizations were performed to understand the phase, morphology as well as chemical compositions. Additionally, zeta potential and BET analysis were performed to obtain clear information on multivalent quinary particles' electrostatic and surface phenomena. Enhanced electrochemical performance of the synthesized HEA consisting of quinary elements, CCNFM, confirmed mesoporous agglomerations providing numerous porous channels *via* its multivalent elements for effective ion intercalation/de-intercalation of the electrolyte ions showing inherent pseudocapacitive contributions. The three-electrode system provided ~386.66 F g^{-1} at the scan rate of 5 mV s^{-1} (264 F g^{-1} at 1 A g^{-1}). Also, the asymmetric liquid state device showed 104.85 F g^{-1} at 5 mV s^{-1} (70 F g^{-1} at 0.5 A g^{-1}) with cyclic stability of ~87% up to 5000 cycles. The above device exhibits an energy density of up to 21 W h kg^{-1} and a power density of 307 W kg^{-1}. From theoretical studies, we could clearly observe the hybridized d-state's contribution near the Fermi level to the capacitance enhancement in the HEA material along with the surface oxidized states.

Conflicts of interest

There are no conflicts to declare.

Acknowledgements

C. S. T. acknowledges a Ramanujan Fellowship, Core Research Grant of SERB, India. STARS project by MHRD India, DAE young scientist award (DAEYSRA) and AOARD (Asian Office of Aerospace Research and Development) Grant no. FA2386-21-1-4014. The project is supported by Kalpana Chawla Space Technology Cell (KCSTC-IIT KGP) Indian Space Research Organisation.

References

1 M. Winter and R. J. Brodd, *Chem. Rev.*, 2005, **105**, 1021.
2 J. Xie, P. Yang, Y. Wang, T. Qi, Y. Lei and C. M. Li, *J. Power Sources*, 2018, **401**, 213–223.
3 L. Kong, M. Cheng, H. Huang, J. Pang, S. Liu, Y. Xu and X.-H. Bu, *EnergyChem*, 2022, **4**, 100090.
4 Y. Tang, J. Ding, W. Zhou, S. Cao, F. Yang, Y. Sun, S. Zhang, H. Xue and H. Pang, *Adv. Sci.*, 2023, **10**, 2206960.
5 H. Zhou, G. Zhu, S. Dong, P. Liu, Y. Lu, Z. Zhou, S. Cao, Y. Zhang and H. Pang, *Adv. Mater.*, 2023, **35**(19), 2211523.
6 L. Miao, Z. Song, D. Zhu, L. Li, L. Gan and M. Liu, *Mater. Adv.*, 2020, **1**, 945–966.
7 M. Kandasamy, S. Sahoo, S. K. Nayak, B. Chakraborty and C. S. Rout, *J. Mater. Chem. A*, 2021, **9**, 17643–17700.
8 A. S. Etman, J. Halim and J. Rosen, *Mater. Adv.*, 2021, **2**, 743–753.
9 M. G. Mohamed, A. F. M. EL-Mahdy, M. G. Kotp and S.-W. Kuo, *Mater. Adv.*, 2022, **3**, 707–733.
10 V. M. Hong Ng, H. Huang, K. Zhou, P. S. Lee, W. Que, J. Z. Xu and L. B. Kong, *J. Mater. Chem. A*, 2017, **5**, 3039–3068.
11 A. Agarwal and B. R. Sankapal, *J. Mater. Chem. A*, 2021, **9**, 20241–20276.
12 S. Chen, Y. Wang, G. Pu, Y. Xue, K. Zhang and Y. Huang, *Energy Fuels*, 2023, **37**, 36–57.
13 W. Dai, T. Lu and Y. Pan, *J. Power Sources*, 2019, **430**, 104–111.
14 M. Sahlberg, D. Karlsson, C. Zlotea and U. Jansson, *Sci. Rep.*, 2016, **6**, 36770.
15 I. Hussain, C. Lamiel, M. Ahmad, Y. Chen, S. Shuang, M. S. Javed, Y. Yang and K. Zhang, *J. Energy Storage*, 2021, **44**, 103405.
16 Y. Wang and Y. Wang, *Nano Energy*, 2022, **104**, 107958.
17 J. Chen, W. Xu, H. Wang, X. Ren, F. Zhan, Q. He, H. Wang and L. Chen, *J. Mater. Chem. A*, 2022, **10**, 21197–21250.
18 F. Zhan, H. Wang, Q. He, W. Xu, J. Chen, X. Ren, H. Wang, S. Liu, M. Han, Y. Yamauchi and L. Chen, *Chem. Sci.*, 2022, **13**, 11981–12015.
19 W. Xu, X. Zhao, F. Zhan, Q. He, H. Wang, J. Chen, H. Wang, X. Ren and L. Chen, *Energy Storage Mater.*, 2022, **53**, 79–135.
20 X. Ren, H. Wang, J. Chen, W. Xu, Q. He, H. Wang, F. Zhan, S. Chen and L. Chen, *Small*, 2023, **19**, 2204121.
21 B. Huang, H. Wang, S. Liang, H. Qin, Y. Li, Z. Luo, C. Zhao, L. Xie and L. Chen, *Energy Storage Mater.*, 2020, **32**, 105–114.

22 X. Zhao, L. Mao, Q. Cheng, J. Li, F. Liao, G. Yang, L. Xie, C. Zhao and L. Chen, *Chem. Eng. J.*, 2020, **387**, 124081.
23 L. Xuan, L. Chen, Q. Yang, W. Chen, X. Hou, Y. Jiang, Q. Zhang and Y. Yuan, *J. Mater. Chem. A*, 2015, **3**, 17525–17533.
24 M. H. Tsai, *Entropy*, 2013, **15**, 5338–5345.
25 S. Wang, T. Zhang, H. Hou and Y. Zhao, *Phys. Status Solidi Basic Res.*, 2018, **255**, 1–6.
26 K. Kong, J. Hyun, Y. Kim, W. Kim and D. Kim, *J. Power Sources*, 2019, **437**, 226927.
27 B. Talluri, M. L. Aparna, N. Sreenivasulu, S. S. Bhattacharya and T. Thomas, *J. Energy Storage*, 2021, **42**, 103004.
28 B. Liang, Y. Ai, Y. Wang, C. Liu, S. Ouyang and M. Liu, *Materials*, 2020, **13**, 5798.
29 M. S. Lal and R. Sundara, *ACS Appl. Mater. Interfaces*, 2019, **11**, 30846–30857.
30 Y. Yuan, Z. Xu, P. Han, Z. Dan, F. Qin and H. Chang, *J. Alloys Compd.*, 2021, **870**, 159523.
31 T. Jin, X. Sang, R. R. Unocic, R. T. Kinch, X. Liu, J. Hu, H. Liu and S. Dai, *Adv. Mater.*, 2018, **30**, 1707512.
32 B. Cantor, I. T. H. Chang, P. Knight and A. J. B. Vincent, *Mater. Sci. Eng., A*, 2004, **375–377**, 213–218.
33 P. D. Jablonski, J. J. Licavoli, M. C. Gao and J. A. Hawk, *JOM*, 2015, **67**, 2278–2287.
34 S. Varalakshmi, G. Appa Rao, M. Kamaraj and B. S. Murty, *J. Mater. Sci.*, 2010, **45**, 5158–5163.
35 S. Calderon Velasco, A. Cavaleiro and S. Carvalho, *Prog. Mater. Sci.*, 2016, **84**, 158–191.
36 T. A. Listyawan, H. Lee, N. Park and U. Lee, *J. Mater. Sci. Technol.*, 2020, **57**, 123–130.
37 Z. Wang, C. Wang, Y.-L. Zhao, T.-H. Huang, C.-L. Li, J.-J. Kai, C.-T. Liu and C.-H. Hsueh, *Vacuum*, 2020, **179**, 109553.
38 K. G. Latham, M. Forghani, W. M. Dose, J. A. Allen and S. W. Donne, *Mater. Adv.*, 2021, **2**, 384–397.
39 L.-Q. Mai, A. Minhas-Khan, X. Tian, K. M. Hercule, Y.-L. Zhao, X. Lin and X. Xu, *Nat. Commun.*, 2013, **4**, 2923.
40 G. Kresse and J. Hafner, *Phys. Rev. B: Condens. Matter Mater. Phys.*, 1993, **47**, 558–561.
41 G. Kresse and D. Joubert, *Phys. Rev. B: Condens. Matter Mater. Phys.*, 1999, **59**, 1758–1775.
42 J. P. Perdew, K. Burke and M. Ernzerhof, *Phys. Rev. Lett.*, 1996, **77**, 3865–3868.
43 A. Hjorth Larsen, J. Jørgen Mortensen, J. Blomqvist, I. E. Castelli, R. Christensen, M. Dułak, J. Friis, M. N. Groves, B. Hammer, C. Hargus, E. D. Hermes, P. C. Jennings, P. Bjerre Jensen, J. Kermode, J. R. Kitchin, E. Leonhard Kolsbjerg, J. Kubal, K. Kaasbjerg, S. Lysgaard, J. Bergmann Maronsson, T. Maxson, T. Olsen, L. Pastewka, A. Peterson, C. Rostgaard, J. Schiøtz, O. Schütt, M. Strange, K. S. Thygesen, T. Vegge, L. Vilhelmsen, M. Walter, Z. Zeng and K. W. Jacobsen, *J. Phys.: Condens. Matter*, 2017, **29**, 273002.
44 X. Jin, X. Gu, F. Quan, X. Ran, K. Zhang and A. Mao, *Materwiss. Werksttech.*, 2019, **50**, 837–843.
45 Z. Xu, S. Sun, W. Cui, J. Lv, Y. Geng, H. Li and J. Deng, *Electrochim. Acta*, 2018, **268**, 340–346.
46 W. Ji, W. Wang, H. Wang, J. Zhang, Y. Wang, F. Zhang and Z. Fu, *Intermetallics*, 2015, **56**, 24–27.
47 E. Shen, X. Song, Q. Chen, M. Zheng, J. Bian and H. Liu, *ChemElectroChem*, 2021, **8**, 260–269.
48 H.-J. Qiu, G. Fang, J. Gao, Y. Wen, J. Lv, H. Li, G. Xie, X. Liu and S. Sun, *ACS Mater. Lett.*, 2019, **1**, 526–533.
49 A. H. Phakatkar, M. T. Saray, M. G. Rasul, L. V. Sorokina, T. G. Ritter, T. Shokuhfar and R. Shahbazian-Yassar, *Langmuir*, 2021, **37**, 9059–9068.
50 K. Fang, J. Chen, X. Zhou, C. Mei, Q. Tian, J. Xu and C.-P. Wong, *Electrochim. Acta*, 2018, **261**, 198–205.
51 M. Zhang, Z. Jiang, M. Niu, Y. Sun and X. Zhang, *Wear*, 2022, **508–509**, 204471.
52 K. Chen and D. Xue, *J. Mater. Chem. A*, 2016, **4**, 7522–7537.
53 Y. Wu and C. Cao, *Sci. China Mater.*, 2018, **61**, 1517–1526.
54 S. D. Negedu, R. Tromer, C. C. Gowda, C. F. Woellner, F. E. Olu, A. K. Roy, P. Pandey, D. S. Galvao, P. M. Ajayan, P. Kumbhakar and C. S. Tiwary, *Nanoscale*, 2022, **14**, 7788–7797.
55 J. Dąbrowa, M. Stygar, A. Mikuła, A. Knapik, K. Mroczka, W. Tejchman, M. Danielewski and M. Martin, *Mater. Lett.*, 2018, **216**, 32–36.
56 P. Patel, S. A. Alidokht, N. Sharifi, A. Roy, K. Harrington, P. Stoyanov, R. R. Chromik and C. Moreau, *J. Therm. Spray Technol.*, 2022, **31**, 1285–1301.
57 D. Yang and M. I. Ionescu, *Metal Oxide–Carbon Hybrid Materials for Application in Supercapacitors*, 2017.
58 N. R. Chodankar, H. D. Pham, A. K. Nanjundan, J. F. S. Fernando, K. Jayaramulu, D. Golberg, Y. Han and D. P. Dubal, *Small*, 2020, **16**, 2002806.
59 A. González, E. Goikolea, J. A. Barrena and R. Mysyk, *Renewable Sustainable Energy Rev.*, 2016, **58**, 1189–1206.
60 Y. Gogotsi and R. M. Penner, *ACS Nano*, 2018, **12**, 2081–2083.
61 K. A. Owusu, L. Qu, J. Li, Z. Wang, K. Zhao, C. Yang, K. M. Hercule, C. Lin, C. Shi, Q. Wei, L. Zhou and L. Mai, *Nat. Commun.*, 2017, **8**, 14264.
62 I. Shafi, E. Liang and B. Li, *J. Alloys Compd.*, 2021, **851**, 156046.
63 Z. Luo, L. Liu, X. Yang, X. Luo, P. Bi, Z. Fu, A. Pang, W. Li and Y. Yi, *ACS Appl. Mater. Interfaces*, 2020, **12**, 39098–39107.
64 R. K. Nare, S. Ramesh, P. K. Basavi, V. Kakani, C. Bathula, H. M. Yadav, P. B. Dhanapal, R. K. R. Kotanka and V. R. Pasupuleti, *Sci. Rep.*, 2022, **12**, 1998.
65 T. S. Mathis, N. Kurra, X. Wang, D. Pinto, P. Simon and Y. Gogotsi, *Adv. Energy Mater.*, 2019, **9**, 1902007.
66 J. Ling, H. Zou, W. Yang and S. Chen, *Mater. Adv.*, 2020, **1**, 481–494.
67 S. Zheng, Y. Sun, H. Xue, P. Braunstein, W. Huang and H. Pang, *Natl. Sci. Rev.*, 2020, **7**, 305–314.
68 M. R. Lukatskaya, B. Dunn and Y. Gogotsi, *Nat. Commun.*, 2016, **7**, 12647.
69 Y. Gogotsi, *ACS Nano*, 2014, **8**, 5369–5371.
70 A. Noori, M. F. El-Kady, M. S. Rahmanifar, R. B. Kaner and M. F. Mousavi, *Chem. Soc. Rev.*, 2019, **48**, 1272–1341.
71 F. Zhang, Y. Zhou and H. Li, *Mater. Chem. Phys.*, 2004, **83**, 260–264.

72 M. S. Gouda, M. Shehab, S. Helmy, M. Soliman and R. S. Salama, *J. Energy Storage*, 2023, **61**, 106806.
73 J.-B. Jorcin, M. E. Orazem, N. Pébère and B. Tribollet, *Electrochim. Acta*, 2006, **51**, 1473–1479.
74 Y. Yin, W.-B. Zhang, X.-L. Zhang, M. M. Theint, J.-L. Yang, Z.-Q. Yang, J.-J. Li, S. Liang and X.-J. Ma, *Dalton Trans.*, 2023, **52**, 9005–9016.
75 Y. Yang, B. Chen, J. Chen, L. Hu and M. Hu, *Can. Metall. Q.*, 2022, **61**, 389–397.
76 M. S. Lal and R. Sundara, *Electrochim. Acta*, 2022, **405**, 139828.
77 X. Xu, Y. Du, C. Wang, Y. Guo, J. Zou, K. Zhou, Z. Zeng, Y. Liu and L. Li, *J. Alloys Compd.*, 2020, **822**, 153642.
78 S. Liu, S. Sarwar, J. Wang, H. Zhang, T. Li, J. Luo and X. Zhang, *J. Mater. Chem. C*, 2021, **9**, 228–237.
79 A. Sharma, S. Kapse, A. Verma, S. Bisoyi, G. K. Pradhan, R. Thapa and C. S. Rout, *ACS Appl. Energy Mater.*, 2022, **5**, 10315–10327.
80 I. Hussain, T. Hussain, S. Yang, Y. Chen, J. Zhou, X. Ma, N. Abbas, C. Lamiel and K. Zhang, *Chem. Eng. J.*, 2021, **413**, 127570.
81 A. A. Mirghni, M. J. Madito, T. M. Masikhwa, K. O. Oyedotun, A. Bello and N. Manyala, *J. Colloid Interface Sci.*, 2017, **494**, 325–337.
82 R. Suresh Babu, R. Vinodh, A. L. F. de Barros, L. M. Samyn, K. Prasanna, M. A. Maier, C. H. F. Alves and H.-J. Kim, *Chem. Eng. J.*, 2019, **366**, 390–403.
83 S. Jangu, B. K. Satpathy, M. Raju, C. Jacob and D. Pradhan, *Dalton Transactions*, 2021, **50**, 6878–6888.
84 C. Wu, J. Cai, Q. Zhang, X. Zhou, Y. Zhu, P. K. Shen and K. Zhang, *ACS Appl. Mater. Interfaces*, 2015, **7**, 26512–26521.
85 X. Wang, W. Guo and Y. Fu, *J. Mater. Chem. A*, 2021, **9**, 663–701.
86 A. Amiri and R. Shahbazian-Yassar, *J. Mater. Chem. A*, 2021, **9**, 782–823.
87 Y. Xin, S. Li, Y. Qian, W. Zhu, H. Yuan, P. Jiang, R. Guo and L. Wang, *ACS Catal.*, 2020, **10**, 11280–11306.
88 T. Wang, J. Guo, Y. Guo, J. Feng and D. Wu, *ACS Appl. Energy Mater.*, 2021, **4**, 2190–2200.
89 J. K. Nørskov, F. Studt, F. Abild-Pedersen and T. Bligaard, *Fundamental Concepts in Heterogeneous Catalysis*, John Wiley & Sons, Inc, Hoboken, NJ, USA, 2014.
90 Y. Guan, Y. Cong, R. Zhao, K. Li, X. Li, H. Zhu, Q. Zhang, Z. Dong and N. Yang, *Small*, 2023, 2301276.